Biomed Tech 2013; 58 (Suppl. 1) © 2013 by Walter de Gruyter · Berlin · Boston. DOI 10.1515/bmt-2013-4419

MONITORING BONE DENSITY FROM PATIENTS UNDERGOING TOTAL HIP ARTHROPLASTY USING COMPUTED TOMOGRAPHY AND 3D MODELING TECHNIQUES

Paolo Gargiulo[1,2], Benedikt Helgasson[3], Benedikt Magnússon[1,2], Throstur Pétursson[1,2], Gianluca Mario Izzo[2,4], Gígja Magnúsdóttir[5], Grétar Halldórsson[5], Jan Tribel[6], and Halldor Jónsson Jr.[6,7]

[1]Department of Science and Development, Landspitali University Hospital
[2]Biomedical Engineering Department,Reykjavik University
[3]Institute for Biomechanics, ETH-Zürich, Switzerland
[4] Department of Biomedical Engineering, University Federico II of Naples, Italy
[5]Rehabilitation Clinic Grensás, Landspitali University Hospital
[6]Orthopaedic Clinic, Landspitali University Hospital
[7]Medical Faculty, Iceland University, Reykjavik, Iceland

paologar@landspitali.is

Abstract: *A clinical trial was carried out including 36 volunteer patients which underwent unilateral THA surgery (50% cemented, 50% uncemented). Changes in bone mineral density after the operation are monitored to assess the outcome of the procedure.*
We found age and gender only to be a modest predictor of bone quality for our THA patients and since poor bone quality is known to be associated with a risk of revision surgery it needs to receive a higher weight in our preclinical assessment when choosing between cemented and uncemented THA.

Keywords: *Total hip arthroplasty—Computed tomography 3D models—Bone mineral density—Cemented and uncemented implants.*

Introduction

Total hip arthroplasty (THA) is performed with or without the use of bone cement. The benefit of the cemented procedure is a faster achievement of implant stability compared to an uncemented procedure where the primary implant stability is secured by geometrical interlocking, press fit forces and friction between bone and implant, whilst the secondary stability is additionally secured by bone ingrowths into the surface texture of the femoral component. In the first years post-operatively, uncemented stems are more frequently revised than cemented stems due to periprosthetic fracture. Managing these fractures may create a real challenge for the surgeons because of the poor quality of the surrounding bone [1]. On the other hand the revision surgery for uncemented implants has a higher success rate and generally results in fewer complications than revision surgeries for cemented implants [2]. Presently clinicians are faced with the lack of reliable guidelines when choosing between cemented or uncemented procedures.
At our clinical center orthopedic surgeons chose between the cemented and uncemented THA based on age, sex and general health conditions, however, quantitative preoperative measurements of bone quality have not yet been included in current clinical guidelines. This means that in general patients over 65 years receive cemented implants while the younger and healthy receive uncemented prosthesis. With the aim of improving our healthcare, reducing future costs and developing more thorough clinical guidelines to aid decision making, we have launched a clinical trial at our center where patients undergoing THA are systematically monitored for this purpose [3]. In the present paper we report preliminary results from this project. The specific aims of this part of the study are:

- To quantify pre operative femoral bone quality.
- To compare bone mineral density at two different time points for patients already enrolled in the trial.

Methods

Data were obtained from 36 voluntary patients (20 females and 16 males) undergoing THA surgery for the first time, 18 patients received a cemented - and 18 received a cementless implant. The average age at the moment of surgery is 56 for the males and 62 for the females. The patients are scanned with a *64-slices spiral CT Philips Brilliance* three times in one year: before, immediately after surgery and finally at 52 weeks post-surgery. The CT scanning region starts from the iliac crest and ends at the middle of the femur; slices thickness is 1mm, slice increment is 0.5mm and tube voltage was set to 120KVp. This CT dataset allows a precise 3D reconstruction of the regions of interest.
Commercial software (MIMICS www.materialise.com) was used to segment each femur from CT data. The segmentation was performed on the pre-surgery and post-op CT datasets and was mainly based on opportune thresholds of the CT-HU (Hounsfield Unit). Based on our previous work [4], HU interval for cortical bone was set to 601-1988 HU while the trabecular bone set to 250-600 HU. The CT scan device was pre-calibrated with QUASAR phantom before the pre-operative scans and 1 year later, before the post-op scans using the same CT protocol adopted for all patients A HU to BMD relationship was based on a quadratic function, BMD $[mg/cm^3] = a \times HU^2$

+ b × HU + c, where *a*, *b, c* are calibration coefficients, which were computed from the phantom CT data. The correlation coefficient for this calibration was $R^2 \approx 0.99$ (Fig.1).

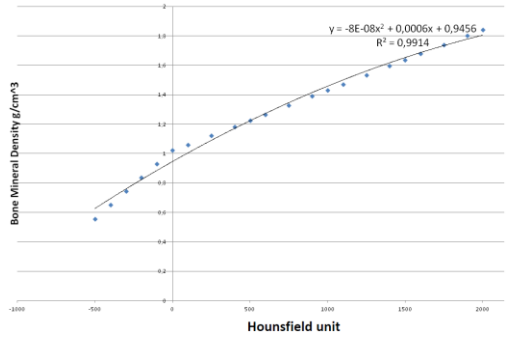

Figure 1: Interpolation of the linear regression curves which is used to convert HU values to BMD.

To estimate the pre-op bone quality, BMD was calculated from the proximal femur volume in the region between femur head and lesser trochanter, along the intertrochanteric line (Fig 2-A). The comparison between pre-op and 1 year post-op BMD cannot be done using the same volume of interest as shown in figure 2-A due to metal artifacts. Thus 2 bone subvolumes were select from the cortical within middle and proximal femur which HU values are minimally influenced by the metal implant artifacts (Fig 2-B).

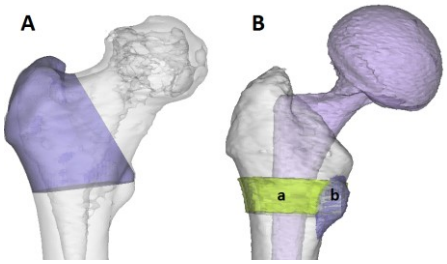

Figure 2: A) The region of interest where the pre-op BMD is computed. B) Regions of interest where BMD pre-op vs. 1 year post-op are compared.

The BMD was measured on the operated femur and on contralateral side (healthy) on the cortical bone from 2 regions in the lesser trochanter area (ROI) minimally influenced by metal artefacts: 2 (indicated with a and b in Fig. 2-B). BMD on these areas is calculated 24 hours and 1 year post surgery.

Results

As expected BMD was generally found to decrease with age but only with a modest negative correlation but this trend was more prominent in men than women (figure 3). The preliminary results from the bone density assessment 1 year post-op are presented in table 1. The BMD variation is positive if the density increases otherwise negative. The decrease in BMD on the treated side was found to range of 1-6% measured at the lesser trochanter. On the contralateral side the BMD remained basically unchanged except in one patient.

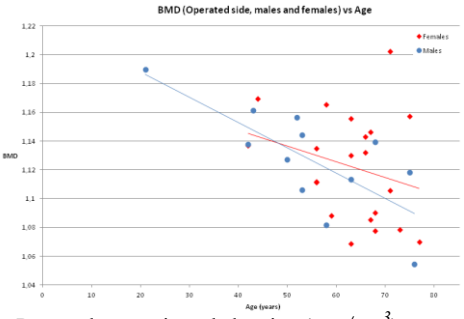

Figure 3: Pre-op bone mineral density (mg/cm^3) vs. age in the region of interest displayed in figure 2A: Comparison of female and male patients.

Table 1: BMD at different time point and relative variation

Patient (Age/gender/implant) OPERATED SIDE	24h Post-Op A	24h Post-Op B	1y Post-Op A	1y Post-Op B	1y/24h A	1y/24h B
21/M/Uncem	1.19	1.34	1.18	1.30	-1%	-3%
52/M/Uncem	1.30	1.38	1.22	1.35	-5%	-2%
56/F/Uncem	1.24	1.41	1.24	1.35	0%	-4%
56/F/Uncem	1.23	1.40	1.21	1.32	-1%	-6%
58/M/Cem	1.24	1.39	1.16	1.32	-6%	-5%
63/F/Uncem	1.16	1.32	1.16	1.31	0%	-1%
63/M/Uncem	1.26	1.38	1.27	1.33	1%	-4%
67/F/Cem	1.24	1.41	1.27	1.34	3%	-5%
68/F/Uncem	1.24	1.32	1.21	1.26	-2%	-5%
77/F/Cem	1.19	1.34	1.20	1.32	1%	-1%
HEALTHY SIDE						
21/M/Uncem	1.22	1.36	1.22	1.38	0%	2%
52/M/Uncem	1.26	1.39	1.26	1.39	0%	0%
56/F/Uncem	1.22	1.39	1.23	1.38	1%	-1%
56/F/Uncem	1.23	1.36	1.24	1.34	1%	-2%
58/M/Cem	1.22	1.34	1.24	1.36	2%	1%
63/F/Uncem	1.12	1.39	1.12	1.31	-1%	-5%
63/M/Uncem	1.21	1.35	1.23	1.35	1%	0%
67/F/Cem	1.16	1.36	1.18	1.36	2%	0%
68/F/Uncem	1.15	1.27	1.15	1.28	0%	1%
77/F/Cem	1.12	1.28	1.12	1.28	0%	0%

Discussion

Our preliminary results indicate the BMD in THA patient in the study is only modestly correlated with age and gender i.e. there is a significant overlap in bone density between age groups and between male and female. We conclude that bone quality assessment will have to be given higher weight in our future treatment protocol for THA patients.

Acknowledgement

The authors would like to thank Landspítali University Hospital research fund for providing financial support to this project.

Bibliography

[1] Venesmaa, P. K. et. al: Monitoring of Periprosthetic BMD After Uncemented Total Hip Arthroplasty with Dual-Energy X-Ray Absorptiometry—a 3-Year Follow-Up Study. J Bone Miner Res, 16: 1056–1061, 2001.

[2] CA Engh, AH Glassman, WL Griffin, JG Mayer Results of cementless revision for failed cemented total hip arthroplasty Clin Orthop, 235, p. 91,1988

[3] Gargiulo, P et. al: Assessment of Total Hip Arthroplasty by Means of Computed Tomography 3D Models and Fracture Risk Evaluation. Artificial Organs.(April 2013).

[4] Gargiulo, P et. al: Monitoring of muscle and bone recovery in spinal cord injury patients treated with electrical stimulation... Artificial Organs. (35(3):275–281, 2011).

Biomed Tech 2013; 58 (Suppl. 1) © 2013 by Walter de Gruyter · Berlin · Boston. DOI 10.1515/bmt-2013-4420

Skin impedance measurements support ex-vivo penetration studies for topical applied drugs

Simon Schwingenschuh[1], Martin Hajnsek[1], Hermann Scharfetter[2], Ørjan G. Martinsen[3], Katrin Tiffner[1], Christian Dragatin[1], Reingard Raml[1], Anton Mautner[1], Manfred Bodenlenz[1], Frank Sinner[1,4]

[1] HEALTH - Institute of Biomedicine and Health Sciences, JOANNEUM RESEARCH Forschungsgesellschaft mbH Graz, Austria
[2]Graz University of Technology, Institute of Medical Engineering, Graz, Austria
[3]University of Oslo, Department of Physics; P.O. Box 1048 Blindern, 0316 Oslo, Norway
[4]Department of Internal Medicine, Division of Diabetes and Metabolism, Medical University of Graz, Graz, Austria

martin.hajnsek@joanneum.at

Abstract: *Open flow microperfusion can be used to assess the amount of a topically applied drug directly in the skin. Large intra- and interindividual differences in skin properties can lead to biased results. In this study we propose a method based on skin impedance measurements to assess the properties of the skin barrier and thus compensate for varying permeability characteristics.*

Keywords: *impedance, open flow microperfusion, skin penetration, topical drugs*

Introduction

Open flow microperfusion (OFM) is a method for continuous sampling of interstitial fluid (ISF) from various tissues of animals and humans. Subsequent analysis of the OFM samples delivers time resolved profiles of many analytes covering a wide range of molecule sizes and chemical properties (e.g. hydrophilicity, lipophilicity). OFM is based on minimally invasive probes with an exchange area featuring macroscopic openings. During the sampling process the probes are perfused with a carrier fluid which mixes with the interstitial fluid of the target tissue. The exchange of carrier fluid and tissue fluid takes place at a certain equilibrium level that allows to measure specific substances present in the tissue by downstream analysis in the bioanalytical lab. OFM is used to investigate drug penetration and drug efficacy in skin in vivo: a probe is placed in the skin, and the cream containing the active ingredient is applied to the skin site directly above the probe. However, there are large individual differences in skin conditions depending on the location of the test site (e.g. forearm, abdomen thigh) and is also dependant on the subject itself (e.g. skin type, environmental conditions). To correct for these differences that will affect the variability of OFM derived drug profiles a large number of skin donors is necessary to reliably test topical drug penetration. In this study we aimed to investigate whether skin impedance measurements can be used to predict at least some of the skin's permeability characteristics.

Methods

Our study is based on the hypothesis that variations in penetrating drug amounts during dermal OFM sampling can be correlated with variations of the passive electrical parameters of the skin. Fresh human skin from plastic surgery was mounted on an ex-vivo test unit (EVA-CELL, Joanneum Research, Graz) to maintain skin vitality and temperature. Skin impedance of each donor skin flap was assessed by using paediatric ECG electrodes in a 3-electrode setting. The electrodes were attached in an equilateral triangle with a side length of 5 cm. The distance between the electrodes was chosen to be 2.5 cm with an electrode diameter of also 2.5 cm. This symmetrical setup allowed moving the three electrodes types (reference, counter and working electrode) simply by varying reconnection of the electrodes to the potentiostat. Impedance spectroscopy and single frequency measurements were used to assess stratum corneum impedance. Clobetasol-17-proprionate (CP17) was applied topically on the skin flaps characterized with the impedance measurements and the penetration of the drug into the dermis was continuously profiled for 24 h by using dermal OFM sampling.

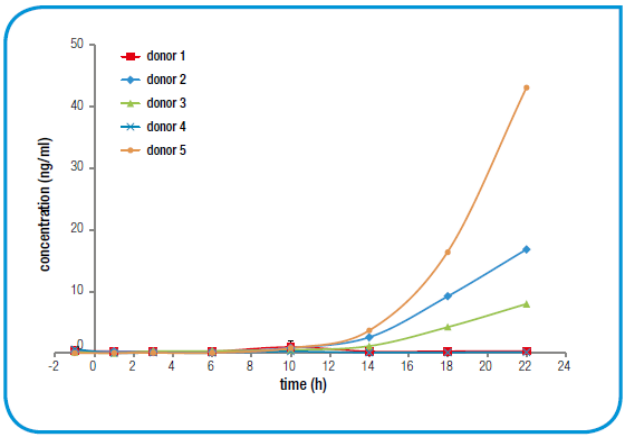

Fig.1: Intradermal concentrations of CP17 in 5 donor skin flaps assessed by continuous sampling using dOFM probes.

Results

To study at what frequencies the skin layers responsible for the barrier function for skin penetration are assessed impedance spectra were recorded from 1000 to 1 Hz with 5 data points per frequency decade. We found that low frequencies below 100 Hz showed a significant correlation to skin penetration properties. The sensitivity of the measurement increases with decreasing frequency which is in good agreement with data from the literature [1]. At higher frequencies also deeper parts of the skin and the subcutaneous tissue contribute to the impedance measured, therefore lower frequencies, which assess only the top layers of the skin, or the stratum corneum only in an optimal case, are more sensitive to penetration properties of the skin.

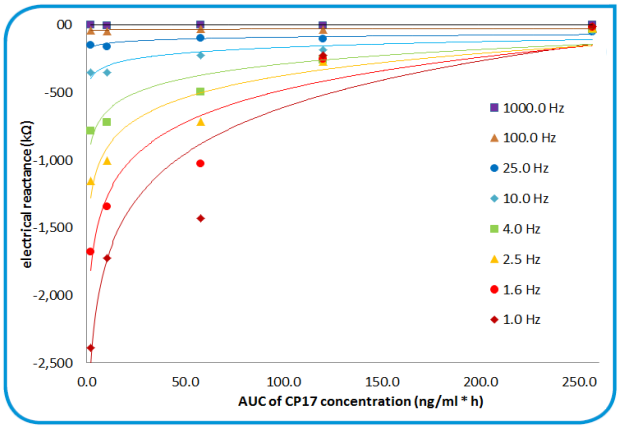

Fig. 2: at low frequencies a significant higher sensitivity to skin penetration properties is observed.

To investigate the relationship between skin impedance and penetrated quantities of CP17, the impedance was plotted against the area under the curve (AUC) of the CP17 concentration over 24 h, a standard measure used in pharmacokinetics. Regression analysis revealed a clear relationship between impedance and the penetrated CP17 amount.

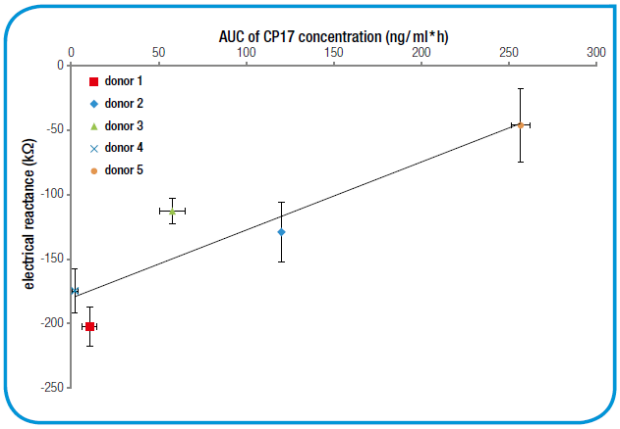

Fig. 3: The electrical reactance shows good correlation with the measured AUC values of CP17 profiles (n=5).

The correlation of skin impedance and drug penetration properties of the skin can be used to normalize dermal OFM AUC values thus eliminating or minimizing the influence of intra- and interindividual differences in skin properties.

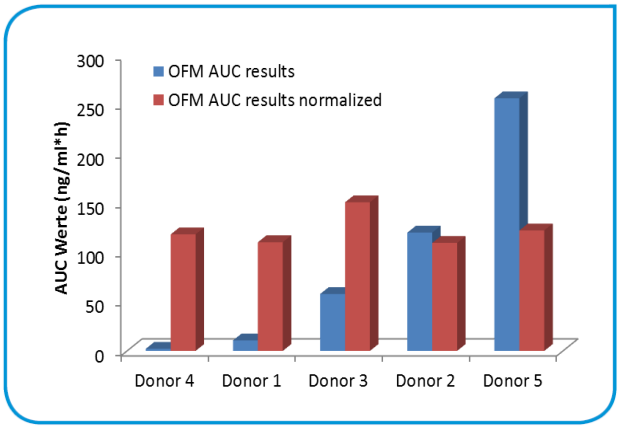

Fig. 3: skin properties variations leading to impedance measurements (n=5).

Discussion

Our results support the hypothesis that the stratum corneum is the main source of variability when testing topical drug penetration into human skin ex-vivo. We conclude that skin impedance measurements can be helpful to characterize skin barrier properties and thus support future ex-vivo and in-vivo skin penetration studies using dOFM sampling. Skin impedance measurements can be used to screen skin properties before OFM studies were performed. Restricting the accepted penetration properties of study subjects to the range representing the population average could significantly reduce the number of subjects needed and thus reduce study costs.

Acknowledgement

The authors acknowledge the Styrian government for financial support via the HTI initiative.

Bibliography

[1] Ørjan G. Martinsen, Sverre Grimnes, Erlend Haug: Measuring depth depends on frequency in electrical skin impedance measurements. *Skin Research and Technology 1999; 5: 179-181*

Biomed Tech 2013; 58 (Suppl. 1) © 2013 by Walter de Gruyter · Berlin · Boston. DOI 10.1515/bmt-2013-4421

RAPID PACING INDUCES FRACTIONATION OF THE ACTIVATION WAVEFRONT INTO MULTIPLE WAVELETS

Hofer E[1], Sanchez-Quintana D[2], Arnold R[1]

[1]Institute of Biophysics, Medical University Graz, Austria
[2]Depart. de Anatomia y Biologia Cellular, Universidad de Extremadura, Badajoz, Spain

ernst.hofer@medunigraz.at

Abstract: *Atrial flutter and atrial fibrillation can be caused by heterogeneities in membrane function as well as in macro- and microstructure. Rapid pacing techniques combined with potential recording techniques can help to localize critical arrhythmogenic substrates within the atrium. This work describes the heterogeneity of local conduction in the cavotricuspid isthmus (CTI) during electrophysiological experiments with Rabbit hearts. By means of rapid pacing techniques it can be shown, that local blockade of excitation spread can be predicted using appropriate pacing protocols. The pre-block behaviour is characterized by a substantial increase in the degree of fractionation and in a decrease of amplitude in extracellular potentials.*

Keywords: *atrial flutter, rapid pacing, complex fractionated atrial electrogram, electrophysiological experiment*

Introduction

Atrial fibrillation and atrial flutter is often preceded by tachycardia. Hence rapid pacing can be used to study the behaviour of cardiac activation before local or global block of excitation spread arises. Increased pacing rate leads to changes in action potential duration and alters the excitation spread. The smooth wave front of depolarization then may break into multiple wavelets with small delays to each other and following complex pathways. These effects are caused by discontinuities in the macro- and microstructure of cardiac tissue. We postulate that during rapid pacing, these effects would lead to increased signal fractionation and spatial heterogeneity, specifically when pacing intervals come close to the absolute refractory period. In electrophysiological experiments with right atria from Rabbits we studied the region of the cavotricuspid isthmus (CTI). Clinical electrophysiologists see this region as one of the targets for catheter ablation to cure atrial arrhythmias [1]. Specific pacing protocols were applied to induce arrhythmogenic conditions. Spatial heterogeneity and beat-to-beat changes of local conduction were analyzed by means of multisite recording techniques of extracellular potentials with ultra-high spatial and temporal resolution [2].

Methods

Electrophysiological experiments were carried out in accordance to the national ethic guidelines. Right atrial specimen were dissected from isolated Rabbit hearts and placed in a tissue bath with oxygenated Tyrode's solution at 36°C. Current pulses of 1 ms duration and twice the threshold level were applied by means of a 50 µm thick tungsten wire at given sites of the tissue. A ramp-like pacing protocol was executed i.e. subsequent stimuli were applied with decreased pacing cycle length (PCL) compared to the previous one until conduction block occurred. Multisite recordings of extracellular signals $\Phi_e(t)$ of the last 6 beats before block were used to analyze the quality of local conduction of the depolarization wave. Amplitude of the signals as well as the fractionation index (FI), i.e. the number of negative deflections of $d\Phi_e(t)/dt$ [3] were used to describe the increasingly hampered excitation process. At least one of the four-electrode-sensors was placed at sites were muscle bundles merge or branch, i.e. at sites of structural discontinuities.

Results

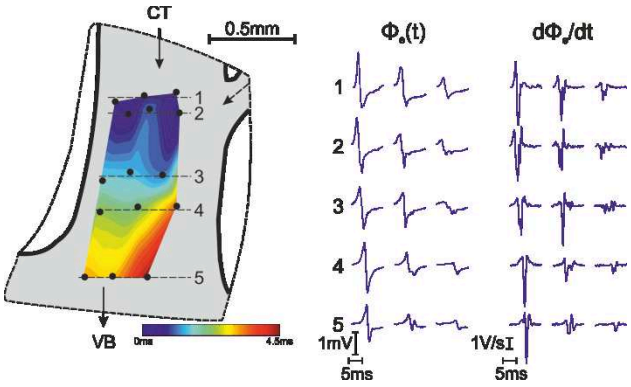

Figure 1: Spatial heterogeneity of depolarization signals within one PectM. Recordings on the right in line 2 and 3 indicate incoming wavelet from the top right branch.

Along the excitation pathway in the CTI, groups of pectinate muscles (PectM) connect the Crista Terminalis (CT) with the vestibule (VB). PectMs branch into two or three fibres and merge again before reaching the VB. At these sites complex signal waveforms with multiple deflections in $d\Phi_e(t)/dt$ can be expected frequently, specifically during rapid pacing close to the block interval. An example of spatial heterogeneity of local signals is depicted in Fig. 1. A map of signals in the lower part of a PectM is shown. Note the small amplitudes and the high degree of fractionation of the signals taken at the right edge of the mapping area. This indicates an electrically uncoupled wavelet entering from the small merging fibre from top right.

Diversity of depolarization signals is not only present in terms of spatial heterogeneity but also at one given recording site in response to subsequent pacing stimuli when PCL decreases. During control values of PCL $\Phi_e(t)$ and $d\Phi_e(t)/dt$ are quite uniform showing a large amplitude and just minor distortion visible as a small secondary deflection in $d\Phi_e(t)/dt$ (see Fig. 2). During the last 6 stimuli before block arises amplitude diminishes and the fractionation index FI increases progressively.

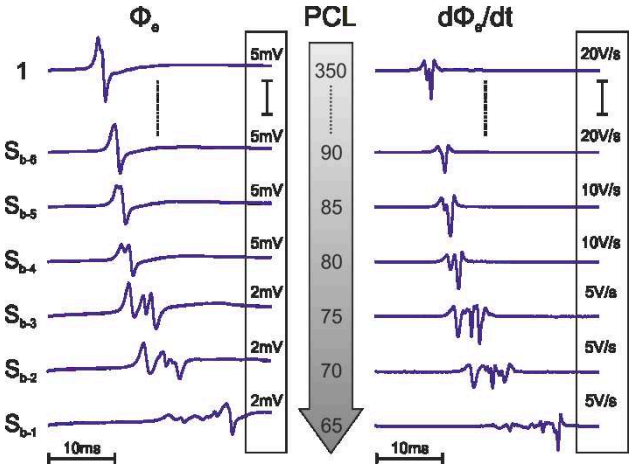

Figure 2: Progressive change of $\Phi_e(t)$ and $d\Phi_e(t)/dt$ with PCL approaching absolute refractory period. Ramp like pacing protocol was used.

We analysed a large number of recordings taken in CT (239), PectM (1037) and VB (264) from 15 hearts. The distribution of FI within each class of tissue differs markedly (see Tab. 1) due to different histological structure. CT represents the most complex microstructure and pathways for the cardiac impulse entering from the sinus node area into the CT resulting in the lowest portion of uniform signals with FI=1. In the class of PectM signals the dominant portion of recordings is uniform. In the VB we found a higher number of uniform signals compared to CT but also a much larger portion of large FI signals (FI=8-10). This might be linked to the fact, that on one hand very compact strands of PectM fibres incorporate smoothly in the VB and on the other hand signals are colliding there with crossing fibres.

Table 1: Fractionation Index distribution obtained in CT, PectM and VB (given in %).

FI	CT	PectM	VB
1	20,51	49,03	46,89
2	26,50	26,56	17,84
3	17,95	11,19	14,11
4	15,81	5,45	5,39
5	8,12	3,60	5,81
6-10	11,11	4,18	9,96

Discussion

Uniform conduction with biphasic extracellular signals along cable like strands of cardiac fibres can be predicted by computer simulation. Within a network of such strands at least piecewise continuous conduction can be expected interrupted just at branching and merging sites representing macroscopic discontinuities. At microscopic scale layers of connective tissue are oriented parallel to the muscle fibres and form obstacles changing the signal waveform with directional effects [4]. By such microstructures the depolarization wave front breaks up into wavelets with delays in the range from 0.5 to 10 ms. It should be emphasized that this type of fractionation is different to those seen in clinical human atrial electrograms with multiple deflections in the range of 50-100 ms. Fractionations like demonstrated here with ultra-high resolution systems (50 µm inter-electrode distances) would not be detectable with relatively coarse recording systems (mm range) like used in clinical electrophysiology.

At a microscopic size scale the CTI can be seen as a network of piecewise cable-like muscle structures producing spatial heterogeneous signals waveforms. In addition to this macro- and microstructure related heterogeneity, temporal parameters like rapid pacing can change the character of local conduction from uniform towards complex and lead to local block and atrial arrhythmia [5]. High resolution recording systems could help to elucidate the mechanisms of complex conduction and improve analyzing techniques to identify zones for ablation.

Acknowledgement

This work has been supported by the Austrian Science Fund (FWF) grant P19993-N15 and grant F3210-N18.

Bibliography

[1] J.A .Cabrera, D. Sanchez-Quintana, J. Farre et al.. "The inferior right atrial isthmus: further architectural insights for current and coming ablation technologies", *J. Cardiovasc. Electrophysiol*., Vol.16, pp. 402-408, 2005.

[2] E. Hofer, F. Keplinger, T. Thurner, T. Wiener, D. Sanchez-Quintana, V. Climent, Plank G. "A new floating sensor array to detect electric near fields of beating heart preparations". *Biosens Bioelectron*., vol. 21(12), pp. 2232-2239, June 2006

[3] T. Wiener, F.O. Campos, G. Plank, E. Hofer. "Decomposition of fractionated local electrograms using an analytic signal model based on sigmoid functions", *Biomed Tech,* pp.1-12, Oct 2012.

[4] F. Campos, T. Wiener, A. Prassl, R. Weber Dos Santos, D. Sanchez-Quintana, H. Ahammer, G. Plank, E. Hofer. "Electro-Anatomical Characterization of Atrial Microfibrosis in a Histologically Detailed Computer Model". *IEEE Trans Biomed Eng.* 2013 Apr 3 (Epub ahead of print).

[5] R. Arnold and E. Hofer, "Pre-block behavior of intra and extracellular parameters during different pacing protocols - preliminary results," in *World Congress on Medical Physics and Biomedical Engineering May 26-31, 2012, Beijing, China,* vol. 39, pp. 395–397, 2012.

Biomed Tech 2013; 58 (Suppl. 1) © 2013 by Walter de Gruyter · Berlin · Boston. DOI 10.1515/bmt-2013-4422

VARIATIONS IN PACING DYNAMICS RESULT IN DIFFERENT HETEROGENEITY AND DEVELOPMENT OF CONDUCTION BLOCK

Arnold R[1], and Hofer E[1],

[1]Institute of Biophysics, Medical University of Graz, Austria

robert.arnold@medunigraz.at

Abstract: *The complex network of muscle fibers in the right atrium is characterized by structural and functional heterogeneities. The influence of these heterogeneities on impulse conduction determines the activation sequence and increases with increasing heart rates. In this work we show that application of dynamic pacing protocols provokes functional heterogeneities and results in ambiguous excitation patterns due to pacing history and structure.*

Keywords: *right atrium, pacing, heterogeneity, cardiac memory*

Introduction

The structural complex muscle network of the cavotricuspid isthmus (CTI) in the right atrium is seen as potential arrhythmogenic substrate [1]. Structural and functional heterogeneities influence excitation spread across the CTI especially at elevated heart rates.

Functional heterogeneities, e.g. restitution of action potential duration (APD) and effective refractory period (ERP), are believed to play an important role in genesis of arrhythmias [2]. Hence, restitution depends on pacing history and pacing dynamics and results in heterogeneous development of local and global conduction block.

Especially in areas where single muscle fibers branch into multiple fibers the electrical source-sink balance is disturbed and the question arises if at elevated heart rates conduction fails earlier in one branch than in the other one. This could create preferred paths for excitation spread with macroscopic re-entry pathways representing substrates for self-sustaining tachyarrhythmias.

In this work we present a methodical approach to provoke and measure regional heterogeneities of conduction block behavior by means of appropriate pacing protocols.

Methods

Tissue Preparation: A guinea pig (weight $\approx 500\,\mathrm{g}$) was anesthetized with $0.4\,\mathrm{ml\,kg^{-1}}$ Ketamin and $0.4\,\mathrm{ml\,kg^{-1}}$ Domidor and sacrificed according to National Ethic Guidelines. The heart was quickly excised and immersed in cold Tyrode solution (4–8 °C). The right atrium with intact sinus node was dissected, pinned down on a transparent silicone carrier, and placed in a tissue bath with warmed (36.4 °C) and oxygenated (95 % O_2, 5 % CO_2) Tyrode solution where it immediately developed autorhythmicity.

Signal recording: Miniaturized flexible sensor arrays comprising 4 Ag/AgCl electrodes in quadratically arrangement with $50\,\mu\mathrm{m}$ edge length [3] were used to estimate the cardiac near field (CNF). The measurement setup and signal recording technique was described in an earlier work [4].

Pacing: Stimulus pulse trains were generated using a custom-written software application (LabVIEW, National Instruments, Austin, Texas) and a FPGA-board (NI PXI-7813R, National Instruments, Austin, Texas). Timing was specified in terms of pacing cycle length (PCL), i.e. the interval in ms between 2 consecutive stimuli [5]. 2 timing characteristics for pacing were used: (i) ramp-like and (ii) stair-like. In ramp-like pacing protocols PCL was reduced after each stimulus, whereas in stair-like pacing protocols PCL was reduced after 15 stimuli at the same PCL. Timing is listed in Tab. 1.

Table 1: Timing of pacing protocols.

Parameter	Ramp	Stair
PCL_{start}	250	250
ΔPCL	5	5
Stimuli at PCL	1	15
PCL_{end}	20	20

Results

Fig. 1 shows the tissue preparation and the location of stimulus and recording sites. Recording site P1 was close to the stimulus site S. Recording sites P2 and P3 were below a branching area on 2 distinct emerging muscle fibers. During stair-like pacing protocol P1, P2, and P3 showed different development of conduction block. In P3 (right muscle branch) conduction failed earliest at a PCL of 70 ms. In P2 (left branch) conduction was sustained until a PCL of 40 ms and in P1 conduction was successful until a PCL of 20 ms (Fig. 2).

In contrast when a ramp-like pacing protocol was applied conduction block occurred at the same PCL (50 ms) at all recording sites (Fig. 3).

Discussion

The preference of specific muscle fibers for excitation spread during high pacing rates favors re-entrant excitation and therefore tachyarrhyhmias. It is known that longitudinal and transversal excitation spread exhibit different block behavior [6]. The complex macro- and microstructure of the CTI dictates the direction of excitation spread and therefore it is likely that individual excitation pathways are preferred.

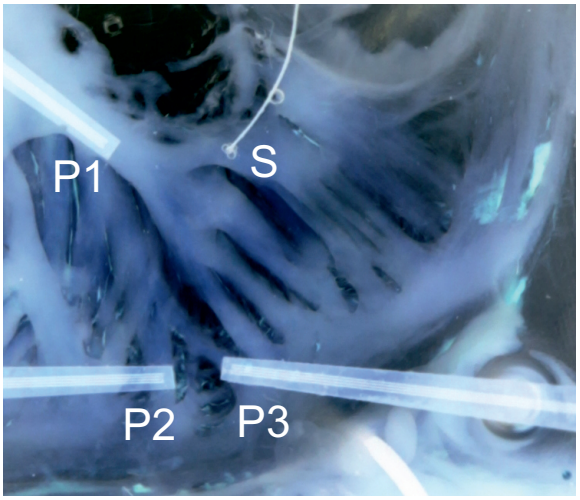

Figure 1: Tissue Preparation. S is the stimulus site, $P_{1..3}$ are the recording sites. P_2 and P_3 are positioned below a branching area.

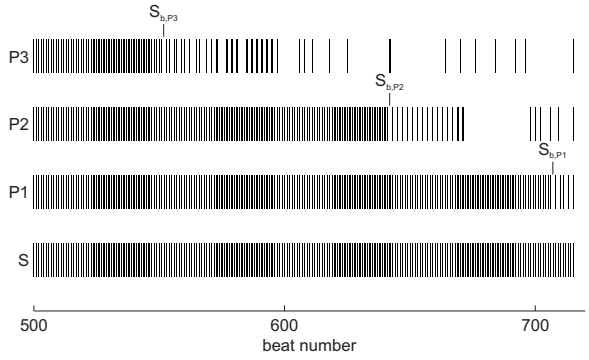

Figure 2: Occurrence and behavior of conduction block for stair-like pacing protocol. Bottom trace (S) is the applied stimulus train, top traces are the evaluated stimulus responses. First conduction block S_b occurs at different pacing intervals in all 3 recording sites.

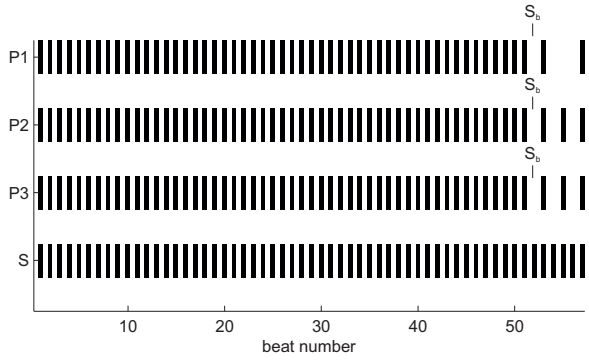

Figure 3: Occurrence and behavior of conduction block for ramp-like pacing protocol. Bottom trace (S) is the applied stimulus train, top traces are the evaluated stimulus responses. First conduction block S_b occurs simultaneously at all recording sites.

Differences in block behavior between the two types of pacing protocols suggest that pacing history and cardiac memory [7] plays a vital role in impulse propagation. A rapid increase in PCL during a ramp-like pacing protocol apparently results in more uniform distributed adaptation dynamics.

It has to be noted that the conduction time between stimulus site and recording sites P2 and P3 is quite large (≈ 35 ms). If PCL is in the same range or below this conduction time correlation between stimulus and activation response is difficult. Nevertheless Fig. 2 and Fig. 3 are valid until first occurrence of conduction block.

Acknowledgement

This work was supported by the Austrian Science Fund FWF under grant P19993-N15 and grant F3210-N18.

Bibliography

[1] J. A. Cabrera, D. Sanchez-Quintana, J. Farre, J. M. Rubio, and S. Y. Ho, "The inferior right atrial isthmus: further architectural insights for current and coming ablation technologies.," *J Cardiovasc Electrophysiol*, vol. 16, pp. 402–408, Apr 2005.

[2] R. H. Clayton and P. Taggart, "Regional differences in apd restitution can initiate wavebreak and re-entry in cardiac tissue: a computational study.," *Biomed Eng Online*, vol. 4, p. 54, 2005.

[3] E. Hofer, F. Keplinger, T. Thurner, T. Wiener, D. Sanchez-Quintana, V. Climent, and G. Plank, "A new floating sensor array to detect electric near fields of beating heart preparations.," *Biosens Bioelectron*, vol. 21, pp. 2232–2239, Jun 2006.

[4] R. Arnold, T. Wiener, D. Sanchez-Quintana, and E. Hofer, "Topology and conduction in the inferior right atrial isthmus measured in rabbit hearts.," *Conf Proc IEEE Eng Med Biol Soc*, vol. 2011, pp. 247–250, 2011.

[5] R. Arnold and E. Hofer, "Pre-block behavior of intra- and extracellular parameters during different pacing protocols - preliminary results," in *World Congress on Medical Physics and Biomedical Engineering May 26-31, 2012, Beijing, China*, vol. 39, pp. 395–397, Springer Berlin Heidelberg, 2012.

[6] M. S. Spach, W. Miller, 3rd, P. C. Dolber, J. M. Kootsey, J. R. Sommer, and C. Mosher, Jr, "The functional role of structural complexities in the propagation of depolarization in the atrium of the dog. cardiac conduction disturbances due to discontinuities of effective axial resistivity.," *Circ Res*, vol. 50, pp. 175–191, Feb 1982.

[7] S. S. Kalb, H. M. Dobrovolny, E. G. Tolkacheva, S. F. Idriss, W. Krassowska, and D. J. Gauthier, "The restitution portrait: a new method for investigating rate-dependent restitution.," *J Cardiovasc Electrophysiol*, vol. 15, pp. 698–709, Jun 2004.

Biomed Tech 2013; 58 (Suppl. 1) © 2013 by Walter de Gruyter · Berlin · Boston. DOI 10.1515/bmt-2013-4423

CONTROL OF A MOBILE REHABILITATION ROBOT USING EXACT FEEDBACK LINEARISATION

Schauer T[1]
[1]Control Systems Group, Technische Universität Berlin, Germany
schauer@control.tu-berlin.de

Abstract: *This contribution is concerned with the feedback control of a table-placed mobile rehabilitation robot using exact feedback linearisation to precisely track arbitrary position and orientation profiles. An outer control loop exactly linearises and decouples the nonlinear kinematic robot model. This loop also generates reference velocities for the three omnidirectional wheels of the robot that are feedback controlled by individual digital controllers on a inner loop level. The concept was validated in simulations.*

Keywords: *Nonlinear Control, Robotics, Rehabilitation*

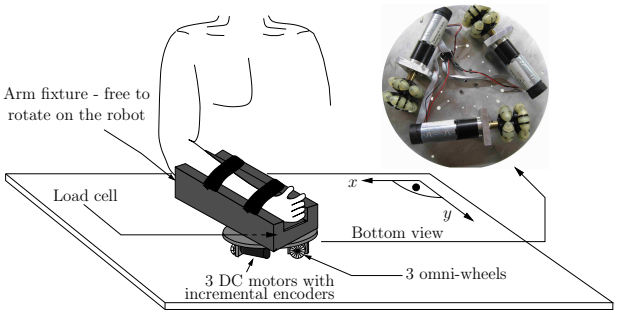

Figure 1: An application scenario of the *Reha-Maus*.

Introduction

Robot-aided neuro-rehabilitation has been widely studied in recent years. A variety of upper limb rehabilitation robots has been developed to assist, enhance, evaluate, and document neurological and orthopaedic rehabilitation of movement. However, these devices exclusively focused on the clinical setting which entails a lack of mobility, high acquisition costs and limited patient training times.

The *Reha-Maus*, which is a novel upper limb rehabilitation system developed by the Control Systems Group at TU-Berlin, represents one of the first concepts of a portable rehabilitation robot that actively provides different levels of patient assistance [1]. The design of the *Reha-Maus* is based on a mobile robot driven by omni-directional wheels. This enables rotational and translation motion in a plane for guiding the hand/lower arm.

However, the previously realised control scheme only allowed the arbitrary tracking of reference positions while the orientation had to be kept nearly constant [1]. Unwanted changes in the orientation, e.g. by external disturbances, could even render the position control loop unstable.

This contribution describes a novel motion control system for the *Reha-Maus* that involves nonlinear control theory in order to enable the generation of arbitrary position and orientation profiles.

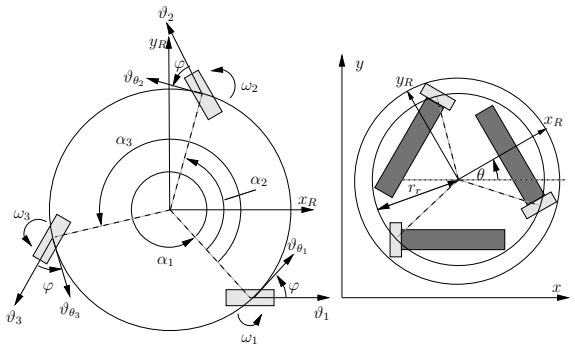

Figure 2: *Reha-Maus*: Geometry and coordinate systems.

Methods

Omni-directional robot and kinematic model

The *Reha-Maus* is designed to allow patients to train their hemiparetic arm. Figure 1 shows a prospective application scenario of the *Reha-Maus*. The lower right arm of a patient is pivoted on the robotic platform. The system is used to assist or resist the patient's arm and shoulder movements during the training. Human-device interaction forces/moments can be measured by a 6D force/torque sensor underneath the arm support, and the movement is monitored by an infrared camera above the table and incremental encoders at the motors. Arbitrary translational and rotational motion on the table surface is facilitated by three DC-motor-driven omni-wheels. More technical details are given in [1].

The *Reha-Maus* possesses three DoFs and has a fixed body frame $[x_R, y_R]$, aligned to the centre of mass (cf. Figure 2). The description of the kinematics and dynamics takes place in generalised coordinates $\boldsymbol{q} = [x, y, \theta]^T$, where x and y represent the position of the robot on the planar workspace and θ is the robot orientation. A kinematic model was derived in [1] based on the assumption that the wheels have no slippage in the direction of traction force. The angular velocities of the three omni-wheels are forming the vector $\boldsymbol{\omega}(t) = [\omega_1(t), \omega_2(t), \omega_3(t)]^T$. The kinematic relation between the wheels' angular velocity vector $\boldsymbol{\omega}(t)$ and the gen-

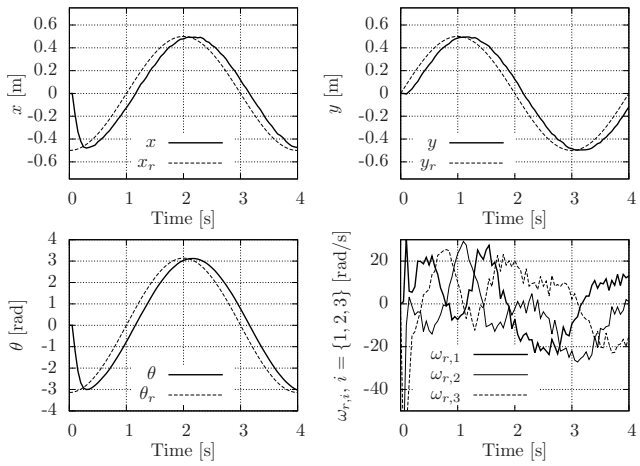

Figure 3: Results for tracking a circular trajectory with simultaneous robot rotation.

eralised velocity vector $\dot{\boldsymbol{q}}(t)$ is defined as

$$\dot{\boldsymbol{q}}(t) = \boldsymbol{\Gamma}(\theta(t))\boldsymbol{\omega}(t) \tag{1}$$

$$\boldsymbol{\Gamma}(\theta(t)) = r_\omega \begin{pmatrix} \cos(\theta) & \cos(\theta + \frac{2\pi}{3}) & \cos(\theta + \frac{4\pi}{3}) \\ \sin(\theta) & \sin(\theta + \frac{2\pi}{3}) & \sin(\theta + \frac{4\pi}{3}) \\ \frac{\sin(\varphi)}{r_r} & \frac{\sin(\varphi)}{r_r} & \frac{\sin(\varphi)}{r_r} \end{pmatrix},$$

where $r_r = 10.5$ cm is the robot rotation radius, and $\varphi = 39°$ is a construction specific angle. The scalar r_ω is the radius of one omni-wheel. A discrete-time kinematic model can be obtained by the Euler method with the sampling period $t_s = 50\,\text{ms}$:

$$\boldsymbol{q}(k+1) = \boldsymbol{q}(k) + \overline{\boldsymbol{\Gamma}}(\theta(k))\boldsymbol{\omega}(k). \tag{2}$$

Here, k is the sample index and $\overline{\boldsymbol{\Gamma}}(\theta(k)) = t_s\boldsymbol{\Gamma}(\theta(k))$.

Control system

To perform arbitrary robot movements, a cascaded discrete-time control structure is applied.

An inner loop consists of three independent motor speed controllers that operate the system at maximum actuator capacity in order to facilitate the simplified state-space description of the robot given below. The sample rate of the inner loop is 1 kHz and a bandwidth of approximately 45 Hz is achieved. The design of each motor speed controller is based on an experimentally identified transfer-function model and is described in [1].

An outer loop regulates the generalised robot coordinates and generates as control signals the reference wheel velocities for the inner loop. The sampling time of the outer loop is set to 50 ms. The relationship between the wheel velocity reference vector $\boldsymbol{\omega}_r$ and controlled wheel velocity vector $\boldsymbol{\omega}$ can be expressed as a simple time delay of one sampling step:

$$\boldsymbol{\omega}(k+1) = \boldsymbol{\omega}_r(k). \tag{3}$$

Combining the kinematic model (2) with the controlled wheel speed dynamics (3) yields a non-linear model with the state $\boldsymbol{x}(k) = [\boldsymbol{q}(k)^T, \boldsymbol{\omega}(k)^T]^T$, the output $\boldsymbol{y}(k) = \boldsymbol{q}(k)$ and the input signal $\boldsymbol{\omega}_r(k)$. This model is employed for designing the outer loop controller. The entire state $\boldsymbol{x}(k)$ is accessible by measurement or estimation [1]. In order to exactly linearise and to decouple the discrete-time multivariable non-linear model, the following relation between the output $\boldsymbol{y}$ and the input $\boldsymbol{\omega}_r$ is derived from the state-space model (Eqs. (2) and (3)):

$$\boldsymbol{q}(k) \quad = \quad \boldsymbol{q}(k-1) + \overline{\boldsymbol{\Gamma}}(k-1)\boldsymbol{\omega}_r(k-2). \tag{4}$$

The control law

$$\boldsymbol{\omega}_r(k) \quad = \quad \overline{\boldsymbol{\Gamma}}^{-1}(k+1)(\boldsymbol{v}(k) - \boldsymbol{q}(k+1))$$

leads to $\boldsymbol{q}(k) = \boldsymbol{v}(k-2)$ with the new input signal $\boldsymbol{v}$. The now linearised and decoupled plant model represents a simple time delay of two sampling steps with respect to signal $\boldsymbol{v}$. The term $\boldsymbol{q}(k+1)$ can be calculated from $\boldsymbol{q}(k)$ and $\boldsymbol{\omega}(k)$ using the state propagation described in Eq. (2). For each generalised coordinate, the exactly linearised plant will be separately feedback controlled by a second order standard linear digital controller with integral action [2] to allow the tracking of a given reference (x_r, y_r, θ_r). The poles of the outer closed-loop dynamics have been chosen to obtain a bandwidth of approximately 2 Hz.

Results

The cascaded control scheme with the nonlinear controller at the outer loop was evaluated in simulations first. Figure 3 shows the results of a tracking test. The robot had to follow a circular path within 4 s while rotating at the same time around its axis. Noise, typically observed at the real system, was added to the states during simulation. The robot was initially in the centre of the circle with an orientation error of 180°.

Discussion

The proposed nonlinear control scheme successfully linearises and decouples the nonlinear discrete-time model and therefore allows the tracking of arbitrary position and orientation profiles. After the compensation of initial errors, the system output follows the references as specified. The observed wheel velocities are feasible in practice. The developed controller forms the basis for the realisation of many therapeutic exercises that will be realised by the robot. The experimental validation of the control concept is ongoing.

Bibliography

[1] D. Lou, T. Schauer, M. Roth, and J. Raisch, "Position and orientation control of an omni-directional mobile rehabilitation robot," in *IEEE Multi-Conference on Systems and Control 2012*, (Dubrovnik, Croatia), pp. 50–56, 2012.

[2] K. J. Åström and B. Wittenmark, *Computer-controlled systems: theory and design*. Prentice Hall, 1997.

Biomed Tech 2013; 58 (Suppl. 1) © 2013 by Walter de Gruyter · Berlin · Boston. DOI 10.1515/bmt-2013-4424

FIRST RESULTS OF A NEW ELECTROMECHANICAL CONTROLLED EXTERNAL VENTRICULAR DRAINAGE IN A PORCINE MODEL

Inga Margrit Elixmann[1], Marian Walter[1], Christine Goffin[1], Michael Czaplik[1], Phil Alexander Huewelmann[1], Monika Kwiecien [1], Martin Weinzierl[2], Markus Oertel[3], Wolfgang-Ingo Steudel[4], Michael Kiefer [3], Berno Misgeld[1], Klaus Radermacher[1] and Steffen Leonhardt[1]

[1]Helmholtz-Institute for Biomedical Engineering, RWTH Aachen University, Aachen, Germany
[2,3,4]Department of Neurosurgery: [2]Helios Klinikum Krefeld, Germany; [3]Inselspital Bern, Switzerland; [4]Saarland University, Homburg, Germany

elixmann@hia.rwth-aachen.de

Abstract: *Acute increase of intracranial pressure (ICP) usually has to be treated with an external ventricular drainage (EVD). Current standard mechanical EVD carry a lot of disadvantages, which hypothetically could be better managed by a newly developed electromechanical EVD. In this report our first preliminary results of such an electromechanical EVD applied in a porcine animal model are presented. The drainage was demonstrated to be both successful in monitoring and controlling elevated ICP, and able to detect slit ventricles due to overdrainage, if the indented target ICP was set too low.*

Keywords: External Ventricular Drainage, Intracranial Pressure, Control, Animal Model

Introduction

An increase in intracranial volume causes raise of intracranial pressure (ICP). Such an increase can occur for example because of an imbalance of the continuous process of production and resorption of cerebrospinal fluid (CSF). Acute high ICP can be life threatening and has to be treated immediately. The standard procedure consists of insertion of a pressure sensor for ICP monitoring as well as a catheter into the ventricles for external drainage of CSF. Usually, the height of the CSF drainage reservoir determines the resulting ICP due to its hydrostatic pressure. This conventional mechanical external ventricular drainage (EVD) has potential disadvantages and possiblities of complications. If the position of the reservoir is chosen too low or the patient changes to an upright position, undesirable overdrainage may occur. The ventricles can collapse to slit ventricles and occlude the catheter perforation. Currently, there is exclusively one commercially available electromechanical EVD consisting of an ICP sensor integrated in the drainage tube followed by a peristaltic pump called Liquoguard® (Moeller Medical GmbH), which is conceived of potentially minimize these problems. However, it is advisable to use this system with an additional independent ICP sensor to be able to detect slit ventricles. If slit ventricles occur, the integrated pressure sensor measures incorrect ICP values [1]. Therefore, the authors developed an innovative electromechanical "intelligent" EVD (iEVD) [2], which measures simultaneously ICP, pressure and flow in the tube and

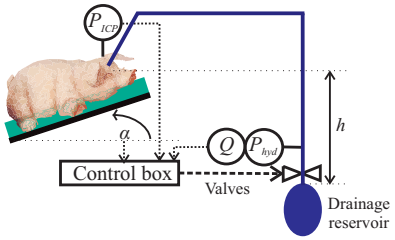

Figure 1: Experimental setup with the iEVD

patient position α (Figure 1). The iEVD functions by a hydrostatic pressure difference between cranium and CSF drainage reservoir and controls the ICP by positioning of a tube squeezer valve and an additional switching valve. It was already tested in an animal experiment, is able to response to changes of the drainage reservoir position or target ICP value and can indirectly detect slit ventricles.

Methods

In the present animal experiment, inducing a kaolin solution into the cisterna magna reduces the pigs's CSF resorption surface. The pig was kept under general anaesthesia. On the third day, the iEVD was implanted and tested.
The control loop with the iEVD is shown in Figure 2. The gradual tube squeezer valve sets an appropriate operating point for the system by adjusting the drainage to the target flow Q_{target} and the switching valve was used in the outer control loop to keep ICP at the intended level. In recent studies, the position of the gradual tube squeezer valve was the only control variable applied. However, due to an integrative error in the position sensor of the tube squeezer valve, the nonlinear relationship of motor position to hydraulic resistance could not be compensated exactly after some time [2] and hence the switching valve was added. A filter uses a 5 s moving window over 100 Hz ICP measurements, determines the maximum (systolic) and minimum (diastolic) ICP value and calculates the average 1 Hz-ICP value by the following equation:

$$ICP = \frac{1}{3}(ICP_{max} + 2 \cdot ICP_{min}) \qquad (1)$$

The control algorithm works with a sample frequency of 1 Hz. At the beginning, the switching valve opens and the

following tube squeezer valve gradually opens in minimal step size of 2.5 µm until the iEVD drains a predetermined target flow Q_{target}. After this initialization the switching valve is controlled with a hysteresis of 0.3 mmHg. While the switching valve is open, a secondary controller increases the stored value of Q_{target} by 50 % if ICP is increasing more than 0.3 mmHg within 1 s or ICP is not decreasing after a certain threshold time.
Whenever $Q_{EVD} < 1.25 \cdot Q_{target}$, the controller increases stepwise the opening position of the tube squeezer valve until Q_{target} is reached.
Slit ventricles are diagnosed when pulsation of the brain is not passed on to the water column and the difference of the maximal and minimal value within a 5 s window of 100 Hz data of the pressure sensor in the drainage tube is smaller or equal to 1 mmHg.

Results

The target ICP had to be chosen higher than 8 mmHg otherwise the pig suffered from slit ventricles (s. Figure 3). With a target ICP of 8 mmHg, slit ventricles occured at approximately t =50 s and at t =56 s the pulsation in the water column P_{hyd} got smaller than 1 mmHg and slit ventricles were identified. The compliance of the tubing dampens the amplitude of ICP by 25 %.
With a higher target ICP the drainage functioned well as shown in Figure 4. At t =110 s the level of the drainage reservoir was increased and the flow decreased. At t =300 s the target ICP was decreased from 10.5 mmHg to 10 mmHg and hence Q_{target} was increased by the controller to drain sufficently. The tube squeezer valve gradually opened the tube until Q_{target} was reached again. After Δt ≈200 s the target flow was constant and only the outer control loop was active once again.

Discussion

First tests of the iEVD at a pig were successful. Potential future improvements could be an automatic increase of target pressure, if slit ventricles were detected. This preliminary iEVD can serve as a platform for more advanced control approaches: Foltz et al. [3] found out that the waveform is more reliable than mean ICP for diagnosis in humans.

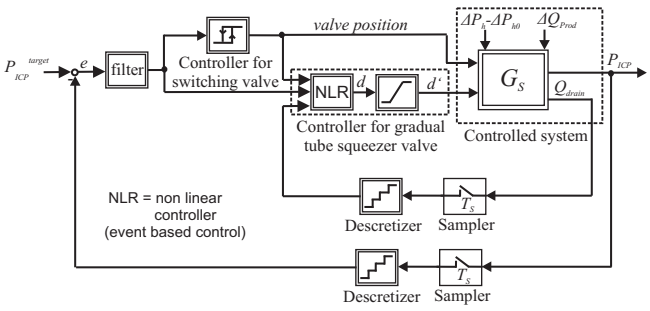

Figure 2: ICP control loop

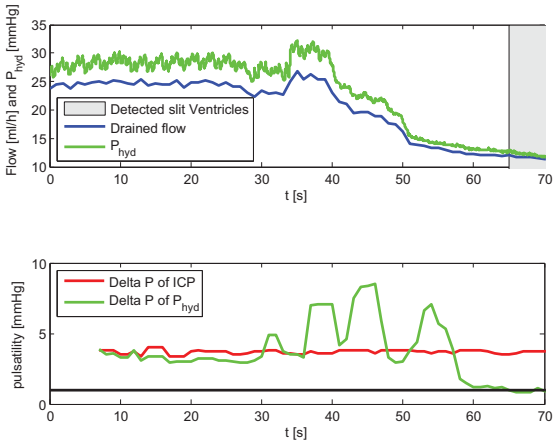

Figure 3: Slit ventricle detection

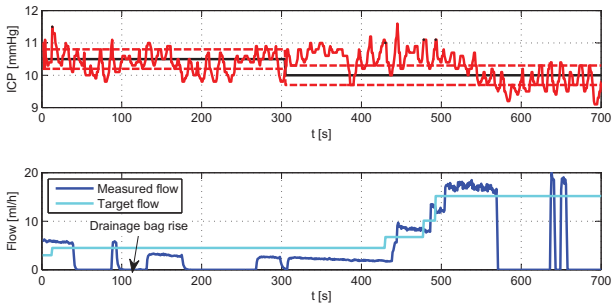

Figure 4: Measured adaption of target flow to maintain the changing target ICP at t =300 s

If pigs show similar single pulse waveform change following increasing ICP, it would be possible to observe how the iEVD performs in draining according to waveform.

Acknowledgement

The authors express their gratitude for the financial support of the BMBF, the support of Sensirion AG and of our project partner Reco Medizintechnik Wolfgang Rentsch e.K. and Raumedic AG.

Bibliography

[1] S. Linsler, M. Schmidtke, W. I. Steudel, M. Kiefer, and J. Oertel, "Automated intracranial pressure-controlled cerebrospinal fluid external drainage with LiquoGuard®," *Acta Neurochir (Wien)*, Nov. 2012, Epub.

[2] I. M. Elixmann, M. Walter, C. Goffin, S. Hahne, M. Kiefer, and S. Leonhardt, "Hirndruckmodellierung und Regelung einer neuen mechatronischen externen Ventrikeldrainage," *at - Automatisierungstechnik*, vol. 59, pp. 613–621, Oct. 2011.

[3] E. L. Foltz and C. Aine, "Diagnosis of hydrocephalus by CSF pulse-wave analysis: a clinical study.," *Surg Neurol*, vol. 15, pp. 283–93, Apr. 1981.

Biomed Tech 2013; 58 (Suppl. 1) © 2013 by Walter de Gruyter · Berlin · Boston. DOI 10.1515/bmt-2013-4425

MODEL-BASED VENTILATOR SETTINGS IN PRESSURE CONTROLLED VENTILATION

Schranz C[1], Becher T[2], Schädler D[2], Weiler N[2], Möller K[1]

[1]Institute of Technical Medicine, Furtwangen University, Germany
[2]Dept. of Anesthesiology and Intensive Care Medicine, University Medical Center Schleswig-Holstein, Germany

scc@hs-furtwangen.de

Abstract: *Mathematical models of respiratory mechanics can be used to optimize ventilatory settings. This paper presents an approach to calculate patient-specific ventilator settings during pressure controlled ventilation. The proposed algorithm identifies the 1st Order Model of respiratory mechanics and calculates ventilator settings that provide a defined alveolar minute ventilation with minimal inspiration pressure and allow sufficient expiration time to avoid the build-up of intrinisic PEEP. The results can also be used to visualize the nonlinear relation of ventilation parameters. Retrospective comparison of calculated ventilator settings in clinical data indicated high concordance to clinically optimized ventilator settings. The proposed algorithm and visualization uncovers the nonlinear interaction of ventilation parameters and supports the determination of individualized ventilator settings. The algorithm minimzes inspiration pressure necessary to achieve a predefined minute ventilation, which may be a useful approach in optimizing lung-protective ventilation.*

Keywords: *Model-based Therapy, Optimized Ventilator Setting, Respiratory Mechanics*

Introduction

Mechanical ventilation carries the risk of ventilator-induced lung injury (VILI), caused by excessive stress and strain to the lung tissue [1]. To minimize the risk of VILI, ventilator settings should be adapted to the individual breathing mechanics of the patient. Currently there is no general consensus about the "ideal" ventilation strategy for preventing VILI. However, there is evidence that considering individual lung properties might be beneficial [2]. Thus, mathematical models of respiratory mechanics can be used to quantify the characteristics of the respiratory system leading to personalized optimized ventilator settings [2]. This paper presents an approach to calculate and illustrate the influence of patient-specific ventilator settings during pressure controlled ventilation (PCV) to maintain a preset minute ventilation. Finally, ventilator settings with minimal inspiration pressure and sufficient inspiration and expiration time can be selected to minimize alveolar stress and to avoid the build-up of intrinsic PEEP.

Methods

The alveolar ventilation is the effective part of the applied minute ventilation (MV) penetrating the regions of the lung where gas-exchange occurs. Alveolar ventilation depends on the dead-space volume V_D, the tidal volume V_T and the respiratory rate (RR):

$$\dot{V}_A = (V_T - V_D) \cdot RR \tag{1}$$

V_D can be approximated using the estimated patient's ideal body weight (iBW).

$$V_D = 2\frac{mL}{kg\ iBW} \tag{2}$$

To calculate the required tidal volume to maintain the desired alveolar ventilation, Eq. 1 is rearranged using the inspiration and expiration time (t_I and t_E) to represent RR:

$$V_T = \frac{\dot{V}_A}{RR} + V_D = \dot{V}_A(t_I + t_E) + V_D \tag{3}$$

The tidal volume in Eq. 1 can be simulated by using a patient-specific model of respiratory mechanics and the applied airway pressure as the defined input signal.

Respiratory mechanics model: The 1st Order Model (FOM) of respiratory mechanics is a serial arrangement of a resistive element (R) and a compliant compartment (C). The FOM is given as a transfer function:

$$H(s) = \frac{V(s)}{p_{aw}(s)} = \frac{C}{1 + sRC} \tag{4}$$

Model simulation: During PCV a pressure signal according to Figure 1 is applied by the ventilator. The initial phase for $t < t_R$ and can be described as follows:

$$p_{aw,Ramp}(t) = \frac{p_I - PEEP}{t_R} \cdot t \tag{5}$$

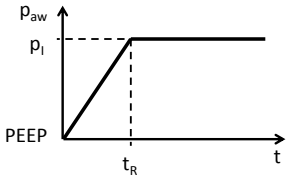

Figure 1: p_{aw} during inspiration phase in PCV

The entire pressure signal during inspiration is constructed by using a step-function $\sigma(t)$:

$$p_{aw}(t) = p_{aw,Ramp}(t) + \sigma(t - t_R)\left[-p_{aw,Ramp}(t) + p_I - PEEP\right] \tag{5}$$

The resulting volume as output signal can be derived in Laplace-Domain by multiplying the transfer function and the Laplace-transferred input signal:

$$V(s) = L\{p_{aw}(t)\} \cdot H(s) \tag{6}$$

By an inverse Laplace-Transformation the resulting tidal volume can be derived in the time-domain for $t > t_R$.

Table 1: Patient characteristics with applied ventilator settings (t_R = 0.2 s) together with identified model parameters and calculated ventilator settings (t_R = 0.2 s).

Pat.	Height	Diagnosis	*alv.Vent (L/min)*	$p_{I,Set}$ *(cmH$_2$O)*	*PEEP (cmH$_2$O)*	$t_{I,Set}$ *(s)*	$t_{E,Set}$ *(s)*	*R (cmH$_2$O·s/L)*	*C (mL/cmH$_2$O)*	τ_E *(s)*	$p_{I,Calc}$ *(cmH$_2$O)*	$t_{I,Calc}$ *(s)*	$t_{E,Calc}$ *(s)*
1	170	Trauma, mod. ARDS	7.0	30.0	15.0	2.0	3.0	14.5	51.2	0.92	29.1	1.5	2.8
2	163	Gold IV Sepsis	5.9	25.0	7.0	0.8	1.8	15.6	25.9	0.45	20.7	0.9	1.4

$$V_T = V(t = t_I) = \frac{C}{t_R} e^{-\frac{t_I}{RC}} (PEEP - p_I) \left[RC \left(e^{-\frac{t_R}{RC}} - 1 \right) - t_R e^{\frac{t_I}{RC}} \right] \quad (7)$$

Calculating ventilator settings: To find the relation of inspiration pressure and inspiration time to meet the calculated tidal volume in Eq. 3, Eq. 7 is rearranged in terms of inspiration pressure.

$$p_I = \frac{RC^2 \left(e^{\frac{t_R}{RC}} - 1 \right) PEEP - t_R e^{\frac{t_I}{RC}} (C \cdot PEEP + V_T)}{C \left[RC \left(e^{\frac{t_R}{RC}} - 1 \right) - t_R e^{\frac{t_I}{RC}} \right]} \quad (8)$$

Patient-specific ventilator settings with respect to sufficient expiration time require an expiration time being at least three times the time constant during expiration τ_E [3]. Thus, p_I is calculated for for two different $t_E = 3 \cdot \tau_E$ and $t_E = 4 \cdot \tau_E$ and two different t_R, being 0 and 0.2 s for various t_I in the range of 0.1 to 4 s.

Model identification: The patient-specific parameters R and C were determined by fitting the FOM to inspiratory data of measured PCV-cycles using multiple linear regression method. τ_E is estimated by fitting an exponential function to the expiratory flow data.

Analysis of clinical data: Data sets of two ventilated patients in PCV from a previous clinical trial were used for this analysis (Table 1). Written informed consent had been obtained from the patients. The clinical ventilator settings had been optimized by experienced ICU-physicians to provide a clinically acceptable minute ventilation with minimal p_I while avoiding the build-up of intrinsic PEEP. The recorded data were used to identify the model as described and the algorithm calculated ventilator settings that would yield the same alveolar minute ventilation.

Results

After estimating R, C and τ_E of the ventilated patients (Table 1), the nonlinear relation between the ventilator settings of p_I and t_I for t_E = $3 \cdot \tau_E$ and $4 \cdot \tau_E$, and t_R = 0.0 s and 0.4 s were obtained (Fig. 2). Obviously, these relations show a unique minimum for p_I. Longer t_E and longer t_R lead to higher p_I to maintain the same alveolar ventilation. Additionally, the effect of t_R on p_I is more dominant in regions of shorter t_I and gets smaller with increasing t_I. The clinical settings in Patient 1 (Fig. 2, left) indicate, that the patient was ventilated with t_E being in the region of $3 \cdot \tau_E$. To minimize p_I, t_I could be reduced from 2.3 to 1.8 s. Patient 2 (Fig. 2, right) was ventilated with $t_E \approx 4 \cdot \tau_E$. The applied p_I could be decreased from 25 cmH$_2$O to 21 cmH$_2$O by shortening t_E to $3 \cdot \tau_E$ and t_I from 1.4 s to 0.9 s.

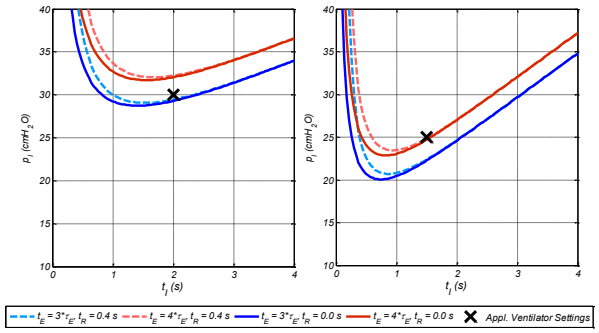

Figure 2: Patient-specific relation of ventilator settings. p_I over t_I to achieve a defined alveolar ventilation, for various t_E and t_R (left: Patient 1, right: Patient 2)

Discussion

The methodology proposed offers clinically acceptable patient-specific suggestions of ventilator settings that are directly applicable at the ventilator. The settings at minimal p_I could be considered as lung-protective as mechanical stress may be minimized and additionally the risk of intrinsic-PEEP build-up is reduced. The visualization of the nonlinear interaction of ventilator settings can be helpful for the clinician to get an impression on the quality of ventilation and to find a direction for further optimization to following therapeutic goals. The nonlinear relation of ventilation parameters becomes transparent and may support the determination of optimized ventilator settings that consider the individual lung physiology.

Acknowledgement

This research was supported by the German Federal Ministry of Education and Research (WiM-Vent, Grants 01IB10002D and 01IB10002F).

Bibliography

[1] J. D. Ricard, D. Dreyfuss *et al.*, "Ventilator-induced lung injury," *Curr Opin Crit Care,* vol. 8, no. 1, pp. 12-20. 2002.

[2] S. E. Rees, C. Allerød *et al.*, "Using physiological models and decision theory for selecting appropriate ventilator settings," *J Clin Monit Comput,* vol. 20, no. 6, pp. 421-9, Dec. 2006.

[3] M. S. Lourens, B. van den Berg *et al.*, "Expiratory time constants in mechanically ventilated patients with and without COPD," *Intensive Care Med,* vol. 26, no. 11, pp. 1612-8, Nov. 2000.

Biomed Tech 2013; 58 (Suppl. 1) © 2013 by Walter de Gruyter · Berlin · Boston. DOI 10.1515/bmt-2013-4426

CURRENT DEVELOPMENTS IN AUTOMATIC DRUG DELIVERY IN ANESTHESIA

Simanski O[1], Sievert A[1,2], Janda M[3], Bajorat J[3]

[1]Automation and Mechatronics Group, Hochschule Wismar - University of Applied Sciences: Technology Business and Design, Wismar, Germany
[2]Institute of Automation, University of Rostock, Rostock, Germany
[3]Clinic of Anaesthesiology and Intensive Care, University of Rostock, Rostock, Germany

olaf.simanski@hs-wismar.de

Abstract: *The main objectives during general anaesthesia are adequate level of hypnosis, analgesia, relaxation, and stable vital functions. During the last 20 years many controllers for the automatic drug delivery in anaesthesia were developed. Our group also developed controllers for the neuromuscular blockade, the depth of hypnosis and the analgesia. In order to administer the medication as needed, a model-based control design or a model-based control is a goal worth striving for. The controller designed in our group and first results of the studies are presented and evaluated briefly.*

Keywords: *automation in anaesthesia, automatic drug delivery*

Introduction

In clinical practice anaesthesiologists have to observe and control a huge amount of hemodynamic and respiratory variables as well as clinical signs for adequate hypnosis and analgesia. In neuro-, thoracic- and abdominal surgery a continuous neuromuscular block is needed to guarantee optimal surgical conditions. A neuromuscular blocking drug is administered in order to prevent reflex muscle movement.
New short-acting drugs are introduced over the last years. This makes a continuous mode for drug application possible and implies the use of automatic control.
For the design of a closed-loop control system a measurable control value and remote controllable infusion pumps are needed.

Measurement and Modelling

For the determination of the degree of neuromuscular blockade is the muscle response recorded. The evoked muscle response after supramaximal stimulation of a motoric nerve (e.g. ulnaris nerve - adductor pollicis muscle) can be registered by electromyography (EMG) or acceleromyography (AMG). A frequently used device is the "NMT-module" (Fa. General Electric) [1].
Measuring depth of hypnosis is often discussed and no final answer can be given. Different algorithms are known for estimation the depth of hypnosis from the raw EEG.
The bispectral index (BIS) becomes very popular in the last years and has been validated in large studies. The algorithm combines the power spectrum and bispectrum with a burst suppression analysis. The BIS describes a complex EEG pattern within a simple variable. The BIS-monitor (Fa. Aspect Medical) reflects the state of hypnosis with help of an index between 0-100, where 0 represents an isoelectrical EEG.
The main problem of measuring the analgesia level is the loss of parameters, which describe the current status. A rather new commercial device called A.N.I.-Monitor (Fa. MetroDoloris) uses a wavelet transformation of the ECG to gather information about the parasympathetic tone. The A.N.I.-Monitor outputs a simple numeric value with a scale from 0 - 100 to describe the state of analgesia calculated from the hearth rate variability (HRV) [2]. More popular is the use of direct HRV parameters to detect the analgesia level [4].
For the controller design it's desirable to use a model description that explains the interaction between the drug infusion and the measurable effect. The most popular kind to model the drug distribution and elimination are pharmacokinetic-pharmacodynamic (PKPD) models.
Pharmacokinetics describes the dynamic process of drug distribution in the body from the infusion to the concentration in the blood and pharmacodynamics describes the interaction from the blood concentration and the measureable effect [3]. Figure 1 shows the general structure of the PKPD model description.

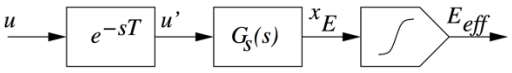

Figure 1: Structure of the simple drug interaction model in Wiener structure, with u as infusion rate, e^{-sT} as delay time for the drug transport, G(s) as transfer function of the PKPD model and E_{eff} as measurable effect after the static nonlinearity.

Depending on the used drug G(s) is a third order model for the neuromuscular blocking drug or a fourth order model for the hypnotic drug Propofol.
Figure 2 shows the schematic description of the developed control system. An adaptive generalized predictive controller (aGPC) was developed for the control of the neuromuscular blockade [5]. Because of the nonlinear behaviour of the measurement of the depth of hypnosis a simple fuzzy controller as nonlinear controller was integrated. For the design of the fuzzy PD+I controller a standard implementation of the integral (I) part was used. The rules for the proportional-

differential (PD) part were designed with the help of the expert knowledge of our anaesthesiologists. A rule-based expert-fuzzy system controls the level of analgesia [4]. It was designed to reflect the decision-making process of anaesthetists regarding the change of infusion rate.

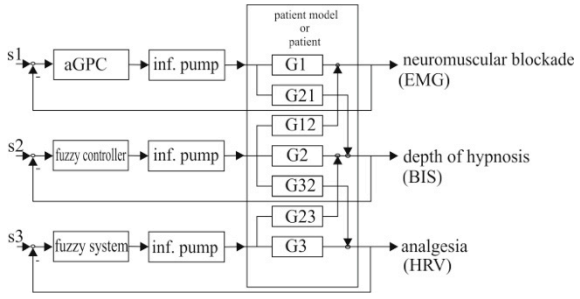

Figure 2: Implementation of the control system at the Control Application Centre at the University of Rostock, with set points s_x and transfer functions G_x and G_{xy}.

Results and Discussion

During the last years different multiple-input multiple-output (MIMO) studies were done [4,5]. Exemplary results show Figure 3 and Figure 4. Figure 3 illustrates one example of a MIMO control of neuromuscular blockade and depth of hypnosis.

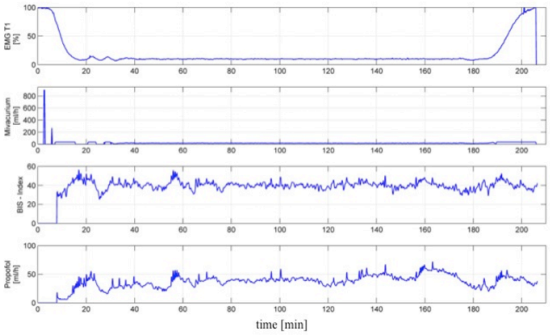

Figure 3: MIMO control study of neuromuscular blockade (NMB) and depth of hypnosis. 1.-plot: NMB-level T1; 2.-plot: drug infusion rate of Mivacurium; 3.-plot: BIS-Index and the last one shows the drug infusion rate of Propofol.

The MIMO control of the depth of hypnosis and the analgesia were also successfully validated. Figure 4 shows an example. The results of both studies were with good performance. These MIMO control system was designed as a decentralized MIMO system. The cross reactions between hypnotic and analgesic drug were interpreted as disturbances. Figure 5 shows a way in which the interaction between hypnotic and analgesic drugs can be modelled. Both drugs can be described with a separate PK model and a common PD model that reflected the interaction of both drugs.

The results of both MIMO control studies show the potential of automatic drug delivery systems to assist the medical staff in the daily work. In near future the control systems should be validated in bigger studies to promote the idea and the development.

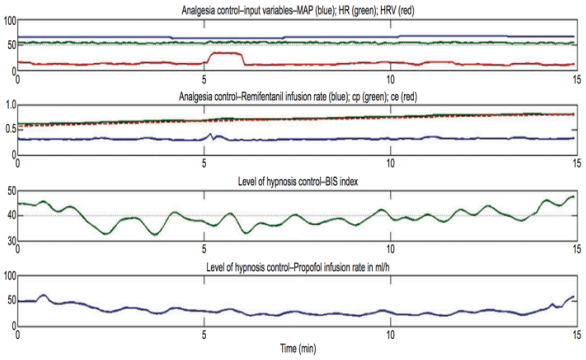

Figure 4; Results of the MIMO study of analgesia and depth of hypnosis. 1.-plot: analgesia parameter, arterial blood pressure (MAP, on the top), heart rate (HR, in the middle), heart rate variability (HRV, on the bottom); 2.-plot: drug infusion rate of Remifentanil (on the top the concentration in blood, on the bottom the rate); 3.-plot: depth of hypnosis level and the last one shows the drug infusion rate of Propofol.

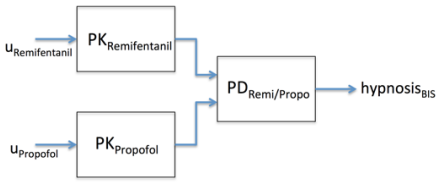

Figure 5: Modelling of the Remifentanil-Propofol interaction regarding to the level of hypnosis.

Bibliography

[1] K. Stadler, "Modeling and control in anesthesia from design to validation." Ph.D. dissertation, ETH Zürich, Institut für Automatik Publikation No.23., 2003.

[2] R. Logier, M. Jeanne, J. De Jonckheere, A. Dassonneville, M. Delecroix, and B. Tavernier, "Physiodoloris: a monitoring device for analgesia / nociception balance evaluation using heart rate variability analysis," in Engineering in Medicine and Biology Society (EMBC), 2010 Annual International Conference of the IEEE, 2010, pp. 1194–1197.

[3] G. T. Tucker, "Pharmacokinetic and pharmacodynamic models," Advances in Pain Research and Therapy, vol. 14, no. 4, pp. 181–201, 1990.

[4] M. Janda, A. Schubert, J. Bajorat, R. Hofmockel, GFE. Nöldge-Schomburg, B. P. Lampe, O. Simanski: Design and implementation of a control system reflecting the level of analgesia during general anesthesia. *Biomedizinische Technik/Biomedical Engineering* 1/2013 pp. 1-12;

[5] M. Janda, O. Simanski, J. Bajorat, B. Pohl, G.F.E Noeldge-Schomburg, R. Hofmockel: Clinical evaluation of a simultaneous closed-loop anaesthesia control system for depth of anaesthesia and neuromuscular blockade Anaesthesia, 2011, doi:10.1111/j.1365-2044.2011.06875.x